Detonation Diffraction in Gases

F. Pintgen [1] J.E. Shepherd *

California Institute of Technology,
Pasadena, California 91125, USA

Abstract

We have experimentally investigated detonation diffraction out of a round tube into an unconfined half-space. The focus of our study is examining how the extent of detonation cellular instability influences the quantitative and qualitative features of diffraction. Detailed quantitative and qualitative measurements were obtained through simultaneous schlieren imaging, multiple-exposure chemiluminescence imaging, and planar laser-induced fluorescence imaging of OH molecules. Two types of stoichiometric mixtures, highly diluted H_2-O_2-Ar and H_2-N_2O, were studied in the sub-critical, critical and super-critical regime. These mixture types represent extreme cases in the classification of cellular instability with highly diluted H_2-O_2-Ar mixtures having very regular instability structures and H_2-N_2O having very irregular instability structures. The most striking differences between the mixtures occur in the sub-critical and critical regimes, for which the detonation fails to transition into the unconfined half-space. For the H_2-O_2-Ar mixture, the velocity on the center line was found to decay significantly slower than for the H_2-N_2O mixture. In case of the H_2-O_2-Ar mixture, it was evident from simultaneous schlieren-fluorescence images that the reaction front was coupled to the lead shock front up to 2.3 tube diameters from the exit plane. For the H_2-N_2O mixture, the reaction front velocity decreased to 60% of the corresponding Chapman-Jouguet value at 1.1 tube diameters from the tube exit plane. A geometric acoustic model showed that the observed differences in failure patterns are not caused by the differences in thermodynamic properties of the two mixtures but is linked to the larger effective activation energy and critical decay time in the H_2-N_2O mixture as compared to the H_2-O_2-Ar mixture. The re-initiation events are similar for the two mixtures and are a consequence of local fluctuations at random locations within the region between the lead shock and decoupled reaction zone, resulting in strong transverse detonations sweeping through shocked but largely unreacted gas.

Key words: Detonation diffraction, cellular instability
PACS: 47.70.Pq, 47.40.Rs, 82.33.Vx

* Corresponding author
California Institute of Technology
Mail stop 105-50
1200 E California Blvd
ph: (626) 395 3283
fax: (626) 395 2900
email: joseph.e.shepherd@caltech.edu
[1] currently at General Electric Global Research, Energy and Propulsion Technologies, Niskayuna NY

Nomeclature

α	Angle of corner disturbance relative to tube axis
β	Mixture dilution amount
c	sound speed
χ	detonation stability parameter
d	tube diameter
Δ	reaction length scale
E_a	activation energy
λ	detonation cell width
P	pressure
R	gas constant
t	time
$t_{d,c}$	critical decay time
T	temperature
θ	nondimensional activation energy
u	gas velocity, lab frame
U	shock or detonation front speed
v	transverse disturbance wave speed
w	gas velocity, wave frame
x	distance

Subscripts

c	critical
i	induction zone
e	energy release zone
CJ	Chapman-Jouguet
TEP	Tube exit plane
ps	post shock
0	initial state

1 Introduction

Diffraction of a detonation from a tube or channel into an unconfined volume leads either to a quenching of the detonation wave, the sub-critical case, or a successful transition and re-establishment of the detonation, the super-critical case. This behavior is not unique to gaseous detonations but also found in liquid and solid-phase detonations [1]. The outcome is determined by the mixture composition, thermodynamic conditions, detonation velocity at the tube exit, the geometry of the area expansion and tube cross section. The transition point from the sub- to the super-critical experimental outcome is known as the critical condition. For the simplest case of a wave propagating close to the Chapman-Jouguet (CJ) velocity and diffracting out of a round tube, there is a well-defined "critical tube diameter" d_c for a given mixture. A super-critical outcome occurs for $d > d_c$ and a sub-critical outcome is observed for $d < d_c$. For gases, this behavior was first discovered by Zel'dovich et al. [2] and subsequent investigations [3–5] demonstrated that the critical tube diameter was a measure of detonation sensitivity that could be correlated with other detonation dynamic parameters [6,7]. For a range of fuel-oxidizer combinations, d_c was found to be strongly correlated [8] with detonation cell width λ or reaction zone length Δ_i [9]. These initial observations [3,4,8] showed that critical tube diameter for a spherical expansion was found to be approximately 13λ for a variety of hydrocarbon-air and oxygen mixtures and detonation waves traveling close to the CJ velocity.

Subsequent studies showed that the 13λ-correlation breaks down for mixtures with increasing argon dilution and values of the critical tube diameter of up to 30λ were measured [10–13] for 80% argon. These mixtures exhibit a more regular multi-front detonation structure than the hydrocarbon-air mixtures, for which highly irregular structure including sub-structure within a detonation cell is observed on soot-foils. Due to the subjective nature of cell width data, especially for highly irregular cellular patterns, the correlations between cell size and d_c have substantial uncertainty. However, there are clear differences in the d_c/λ correlation for different mixtures that are associated with systematic differences in the cellular regularity in fully developed detonations and can not be ascribed to the uncertainties in λ [14]. Correlations of critical tube diameter with the idealized one-dimensional reaction zone length [9,11,15] also show these trends. Computations of the steady reaction zone based on the Zeldovich-von Neumann Döring (ZND) model with detailed chemical reaction models can be used to define parameters that correlate with the extent of cellular regularity. One of the key parameters is the non-dimensional effective activation energy $\theta = E_a/RT_{ps}$ which can be computed from detailed chemical reaction mechanisms [11,16] and used to characterize the observed degree of cellular regularity [17,18]. The effective activation energy for the mixtures with regular structure is significantly lower than for mixtures with

highly irregular structure [19,20]. Another parameter is the ratio of the length of the energy release region compared to the induction zone length [21]. The energy release region is significantly broader (relative to the induction zone length) for mixtures with regular structure [21] than for irregular structure. Associated with irregular detonation structure are large fluctuations in the lead shock strength [22] and consequently, fluctuations in the thermodynamic state within the reaction zone.

Lee [14,7] has proposed that differences in diffraction behavior of mixtures with regular and irregular cellular structure reflects a fundamentally different propagation and failure mechanism in the two cases. Lee argues that in detonations with regular structure, the instability of the detonation is weak and the role of transverse waves is secondary so that the failure mechanism is of the laminar type associated with wave curvature. For detonations with highly irregular structure, Lee argues that the role of transverse waves is primary so that the failure mechanism is due to the decreased frequency of transverse wave intersections and associated high temperature regions if new waves are not formed on the expanding wave front. Another viewpoint is that the failure mechanism is associated with a decoupling of the shock and reaction zone [16,23]. Eckett et al. [16] showed that decoupling will take place when the time scale characterizing the lead shock decay is comparable to a critical shock decay time computed from idealized reaction zone models. The critical decay time in regular mixtures turns out to be substantially smaller than in irregular mixtures, which will result in the failure process being much more abrupt in irregular than regular mixtures, independent of any considerations about transverse waves.

Despite a number of computational studies [24,25,23] of detonation diffraction, the role of transverse waves in diffraction remains unclear. The observed relationship between cellular regularity and diffraction behavior may indicate a link between the extent of fluctuation within the reaction zone and diffraction behavior but this is speculative. One goal of the present study is to provide high resolution images of the events within the reaction zone of diffracting detonation waves that can be used to shed light on the relationship between reaction zone structure, cellular regularity, and detonation diffraction.

The breakdown of the 13λ-correlation is well documented in the literature in terms of the critical tube diameter comparing high and low activation energy mixtures. However, there is a lack of quantitative data and detailed documentation of the diffraction process comparing both mixture types. Since schlieren and chemiluminescence records can be interpreted with a greater confidence in two-dimensional flow, many previous studies employing visualization were carried out in high aspect ratio channels [4,26] rather than a circular tube. These studies of cylindrically expanding detonations also allow the use of soot foils which are the simplest sort of instrumentation. However, recent experi-

ments of fully developed detonations in a narrow channel have shown that the detonation structure remains three dimensional even in narrow channels for highly regular mixtures for which the cell size is much larger than the channel width [27]. The out-of-plane transverse wave structures will reflect from the side walls and may influence the diffraction process, especially in the critical regime. In order to eliminate sidewall effects, the present study [28] was conducted for a circular tube and hemispherically expanding detonations. In our study, we have for the first time applied the simultaneous planar laser induced fluorescence and schlieren technique [29] to directly visualize the reaction front and cellular structure [30,27] evolution during diffraction. We have also simultaneously used multiple exposure chemiluminescence imaging to describe and quantify the different patterns and mechanisms observed for decoupling and recoupling of shock and reaction fronts.

The objective of the present study is to obtain detailed measurements that can be used to provide quantitative data to test the various theories about detonation diffraction and speculations about the role of transverse waves in mixtures with very different degrees of cellular regularity. To this end, we have carried out experiments with two mixtures with extremely different instability characteristics. One mixture, H_2-O_2-Ar has low activation energy and a very regular (laminar) instability structure and the other mixture, H_2-N_2O has a much higher activation energy and a very irregular cellular structure. In addition to the imaging, we offer quantitative data for the wavefront and reaction front shapes and velocities.

2 Experimental Setup

The detonation diffraction facility consists of a 1.5 m long tube with an inner diameter of 38 mm. The tube is attached to the 0.8 m long 150 mm square test section [31] as shown in Fig. 1. The tube end face is located 50 mm upstream of the window center. The tube end face plate attached to the diffraction tube inside the test section reaches to the walls of the test section and creates a rotationally symmetric sharp concave corner of 90°. The corner radius is less than 0.3 mm. The detonation is initiated by an electrical spark (total stored energy of 225 mJ) and a Shchelkin spiral for enhancing the deflagration to detonation transition (Fig. 1). Pressure histories were recorded by a total of six pressure transducers (P1 to P6, Fig. 1) equally spaced in the tube and test section. From time of arrival data, the propagation velocity of the detonation before reaching the area change was measured to be within 2% of the calculated CJ velocity. The experimental facility is described in more detail in [15] and [28].

Three optical diagnostic techniques were used simultaneously: schlieren tech-

nique, planar laser induced fluorescence (PLIF) of the OH radical and multiple exposure chemiluminescence imaging. The test section has two windows opposite to each other, 150 mm in diameter, which allow the parallel schlieren light beam to enter and exit the test section (Fig. 2). The schlieren setup is a classical Z-setup with two parabolic mirrors of focal length 1000 mm. The light source is a ruby laser with a pulse length of approximately 50 ns [32].

The arrangement for flow visualization is shown schematically in Fig. 2 and is described in detail by Pintgen [28]. The test section (see Fig. 2 for the location of the components of the visualization system described in this paragraph) is equipped with a UV-transmitting quartz window in the end plate, which permits the laser light sheet for the PLIF diagnostics to pass through the detonation perpendicular to the direction of propagation. The UV light sheet is formed by the combination of a cylindrical lens ($f = -25$ mm) and a spherical lens ($f = 1000$ mm) before entering the test section. A portion of the fluorescence signal created by the interaction of the UV light with the OH molecules behind the detonation front is imaged in the direction perpendicular to the UV light sheet. The fluorescence passes through the UV-transmitting quartz window on the side of the test section and is filtered by a bandpass filter with a centerline of 313 nm and full width half maximum (FWHM) of 10 nm. The fluorescence is imaged by a 576 $\times$ 384 pixel 12-bit intensified charge-couple device (ICCD) Camera (Princeton Instruments ITE/ICCD-576). The camera was gated by a 30 ns pulse, which allows for a minimization of chemiluminescence as a source of noise. Since the characteristic quenching time is less than 1 ns [28], far smaller than the natural fluorescence life time, the fluorescence signal does temporally coincide with the dye laser pulse of approximately 20 ns length. The image is formed by a 105 mm f/4.5 UV-transmitting Nikkor lens. The height of the imaged region was between 48 and 73 mm depending on the particular experiment.

The lasers used for schlieren and PLIF imaging were triggered by a delay generator connected to the pressure transducer P3. The light output of the excimer-pumped dye laser has a jitter of approximately 200 ns. To overcome this difficulty, an induction coil was placed inside the excimer casing to obtain a highly repeatable gate operation of the ICCD camera with respect to the PLIF light pulse.

For the simultaneous use of the PLIF and schlieren system, the camera had to be moved out of the optical path of the schlieren system. The resulting distortion of the PLIF image was corrected by means of a projective transformation. The PLIF and schlieren images were obtained within 80 ns which allows for an overlay of both images with a minimal displacement of spatial features. To ensure alignment of the superimposed images, a set of target images was used to provide fiducial locations to calibrate the post-processing software.

For most experiments, multiple exposure chemiluminescence images were obtained simultaneously on a 16 bit ICCD camera (Princeton Instruments PI Max) with a resolution of 512×512 pixel. From the multiple images, the average velocity of the leading luminescence front between gate pulses could be determined. One PLIF image, one schlieren image, and one multiple exposure chemiluminescence image could be acquired simultaneously per experiment. The experimental setup and timing of the imaging systems is discussed in more detail in [28].

3 Mixture Characterization

We studied two mixture types that bracket the range of detonation front instability and cellular regularity that has been observed in previous laboratory experiments. Highly Ar-diluted H_2-O_2 mixtures exhibit a very regular cellular structure [19,33], whereas H_2-N_2O mixtures are known as highly unstable with cellular substructure [34]. All mixtures were studied at stoichiometric composition and an initial temperature of 295 K. Three series of experiments, given in Table 1, were performed.

Two of the major parameters characterizing these mixtures are the induction length Δ_i and the reduced effective activation energy $\theta = E_a/RT_{ps}$. These parameters have been used extensively in previous studies on diffraction diffraction [10,11]. The induction zone lengths computed using the ZND model and the maximum thermicity point [35] are (Table 1) between 0.05-0.12 mm for the H_2-O_2-Ar mixture and 0.1-0.18 for the H_2-N_2O mixtures. In terms of the induction zone length Δ_i, the critical diameters are $d_c \approx 530\Delta_i$ for the Ar dilution series and $d_c \approx 230\Delta_i$ for the N_2O series. The values of D/Δ_i (Table 2) are consistent with the results of previous researchers [10,12,13] who showed the strong influence of the cellular regularity on the relationship of critical tube diameter to reaction zone length or cell size.

As described in [16], detailed reaction models and numerical simulation of induction times t_i were used to define an effective value of $\theta = T/t_i \; \partial t_i/\partial T$ by numerically evaluating the derivative of the induction time t_i with respect to the post-shock temperature T at CJ conditions. The differentiation was carried out as described in [16] using a temperature perturbation of $0.01T$ in a constant volume explosion computation and detailed chemical reaction mechanisms [36,37]. Detonations in mixtures with higher values of θ are correlated with a more unstable and more irregular structure [17,18,27]. For the H_2-O_2-Ar mixture, $\theta \sim 5$ and for the H_2-N_2O mixture, $\theta \sim 9.5$, see Table 1.

The shape of the energy release (thermicity) profile has been shown [38,39,21] to also have a strong influence on the stability characteristics. In the present

cases, the width of the energy release region is smaller than the induction zone thickness. The ZND-model [35] was used to calculate the reaction zone structure using detailed chemical reaction mechanisms of Maas and Mueller [36,37]. The ratio of induction length Δ_i to energy pulse length Δ_e is given for both mixtures in Table 2. The energy pulse is approximately one-half the induction length for the H_2-O_2-Ar mixture and about one-quarter the induction length for the H_2-N_2O mixture. As a consequence, the combined stability parameter $\chi = \theta\Delta_i/\Delta_e = 9.3$ for the H_2-O_2-Ar mixture and 36 for H_2-N_2O mixture. The values of χ are consistent with the difference in the regularity of the patterns on the soot foils, see the discussion in [21]

Previous work on shock initiation [16] and detonation diffraction [23] has shown that the concept of a critical shock decay rate can be used to evaluate the sensitivity of the reaction zone to a rapid decrease in shock speed such as that occurring in the diffraction problem. The larger $t_{d,c}$, the more rapid the failure process for a given shock decay rate [16]. The critical shock decay time is computed from a numerical simulation of the modified ZND structure with an approximate model of unsteadiness, described in detail by Eckett et al. [16]. The critical shock decay times $t_{d,c}$ given in Table 2 are approximately 3 times larger in H_2-N_2O mixtures than in the H_2-O_2-Ar mixtures. This implies that the failure process behind the unsteady leading shock wave created during subcritical diffraction events may be much more abrupt in H_2-N_2O mixtures than in H_2-O_2-Ar mixtures. Evidence of this is provided in the next section detailing the results of our experiments.

4 Experimental Results

In our experiments, we have concentrated on the subcritical and critical regimes of diffraction. These are the most interesting from the point of view of examining the mechanisms of detonation failure and the differences between the behavior of detonations with regular and irregular instability structures. Experiments in the subcritical regime provide information on how fast disturbances propagate along the detonation front and how the coupling between leading shock and reaction front is affected by these disturbances. Experiments in the critical regime provide information on how the leading shock and the reaction front eventually re-establish a coupled configuration after being disturbed by the expansion wave propagating along the front. In both regimes, we have obtained extensive imaging data and carried out quantitative analysis of the reaction zone and leading shock features, which are discussed at length in Pintgen [28]. Selected results are summarized in this section.

The diluent amount and initial pressure were found to be parameters that could be conveniently changed in the experiment in order to examine different

diffraction regimes. As discussed in the previous section, for a given mixture, θ is essentially constant and variation of initial pressure and dilution only changes the induction zone length Δ (Table 1). This allows us to study a mixture with a fixed degree of regularity but in different diffraction regimes. Varying the mixture composition enables studying the effect of reaction zone structure and mixture type, ie, regular vs irregular cellular patterns.

A common diagnostic for all experiments was pressure measurements made within the tube (P_1-P_3) and in the test section (P_4-P_6) downstream of the diffraction plane. Representative pressure histories for two tests are shown in Fig. 3. The first three pressure signals P_1 - P_3 (for both cases shown) are shown to demonstrate that a fully developed detonation propagating near the CJ speed is present in the detonation tube prior to the diffraction. This signals show a propagating jump in pressure followed by an expansion wave characteristic of a detonation initiated at the closed end of a tube. The last three pressure signals P_4-P_6 are used to determine if the detonation wave is transmitted downstream.

The pressure histories (Fig. 3) obtained from transducers P_4 (Fig. 1) were used to make a quick determination of whether the detonation successfully transitioned into the test section or detonation failure occurred. If the peak pressure observed on P_4 was smaller than the calculated CJ-pressure, detonation failure was assumed, otherwise the detonation was assumed to have successfully transitioned. An example of the critical regime determination using peak values of P_4 is shown in Fig. 4 for the H_2-O_2Ar mixtures. The exact nature of the diffraction event could then be determined by optical measurements at the exit plane once the diffraction regime was identified for a particular set of mixture conditions. In Fig. 3a, the case is subcritical and a few weak shocks are seen on P_4 but no detonation is evident and the shocks have substantially decreased in amplitude by the time the waves reach P_5 and P_6. In Fig. 3b, the case is supercritical and the leading pressure wave magnitude and timing on P_4-P_6 are consistent with a detonation propagating in the test section.

The range of mixture parameters for which sub-critical and super-critical experimental outcomes are both possible is denoted as the critical regime as shown in Fig. 4. These observations were confirmed by schlieren images and multiple-exposure chemiluminescence images. The interaction of the diffracting detonation wave with the test section confinement [24] was found to have had little effect on the determination of the experimental outcome based on P_4. The side walls of the test section are sufficiently far from the tube exit so that either re-ignition or complete failure has occurred by the time the wave reaches $P4$.

4.1 Subcritical Regime

In the subcritical regime, the leading shock wave is observed to continuously decouple from the reaction front as the diffracted shock moves outward from the tube exit. This is shown in the schlieren images of Fig. 5-6 and the combined chemiluminescence, schlieren, and PLIF images of Fig. 7. In all cases, the detonation is moving left to right so that the diffraction plane is on the left hand side of images. For the H_2-O_2Ar mixtures, Fig. 5, the leading shock front remains coupled to the reaction front on the axis of symmetry for a longer distance than observed for the H_2-N_2O mixtures, Fig. 6. The decoupling in the case of H_2-N_2O mixtures takes place fairly uniformly over the entire shock surface. In the case of the H_2-O_2-Ar mixtures, the reaction front is closer to the shock along the axis of symmetry than near the exit plane.

The images sequences shown in Figs. 5 and 6 are from separate experiments carried out with variable delay times between the image acquisition and detonation arrival at the diffraction plane. The experiments are quite repeatable overall but the fine details of the transverse wave structure and failure process are slightly different from shot-to-shot. In order to remove this variability, a set of multiple images of the OH chemiluminescence was obtained as a function of time for each shot. This was done using a special ICCD camera that could take up to 15 images separated in time by 3 to 6 μs with an exposure time of less than 200 ns. These images are shown in Figs. 5a and 6e. All of the images for a given test are superimposed since the electronic shutter of a single ICCD chip is opened multiple times during the diffraction event. As a consequence, the intense chemical reaction behind the active detonation front is observed as a set of slightly curved vertical bands with diminishing height as the wave propagates away from the exit plane at left-hand side of the image. Since the detonation fails in these two cases, the chemiluminescence disappears by the time the detonation leaves the field of view. The chemiluminescence persists for the H_2-O_2-Ar mixtures further from the tube exit plane than for the H_2-N_2O mixtures, as seen on multiple exposure chemiluminescence images of Fig. 7a) and e).

In order to examine the relationship between the shock front and the chemical reaction zone, simultaneous schlieren (Fig. 7 b) and f) and PLIF (Fig. 7 d) and fh) images were also obtained in a single experiment. The PLIF image was obtained over a slightly smaller portion of the wave than the schlieren image as shown by the red box on Fig. 7 b) and f). The PLIF images are rendered in false color, brought into precise spatial registration with the schlieren images, corrected for optical distortion, and overlaid on the cropped schlieren images in Fig. 7 c) and g). A clear separation between the region of high OH concentration and the shock front can be observed at the top and bottom of the images where the shock strength is the lowest. The reaction zone can also be

observed to suddenly break away or decouple from the shock front a location just off the tube axis (center of the image) on Fig. 7c.

Comparing Figs. 7 c) and g), we see that the decoupling process is faster for the H_2-N_2O mixtures than H_2-O_2-Ar mixtures. The distance between lead shock and reaction front, as marked by the OH-front, is larger for the H_2-N_2O than for the H_2-O_2-Ar mixtures, particularly near the tube axis. The OH front is not smooth but shows the corrugations characteristic of propagating detonations. This can be seen in all the PLIF images we have obtained (for example, the OH fronts in Fig. 11, 12, and 15). The corrugated structure of the OH front was discovered by Pintgen [29] and described by Pintgen et al [30] for H_2-O_2-Ar mixtures and other mixtures by Austin et al. [27]. The spatial structure of the OH front can be explained by the sensitivity of the reaction rates to temperature and the fluctuations of leading shock speed and post shock temperature due to detonation instability, as discussed in detail by Pintgen et al. [30].

In the case of H_2-O_2-Ar mixtures, the spatial structure is nearly periodic and the OH front contains keystone-shaped features [30]. In the case of H_2-N_2O mixtures, the structure of the front is much more irregular and a wide range of length scales [17,18,27] is created by detonation instability. The largest characteristic dimension of spatial features on the OH front is related to the detonation cell size λ. As measured on the detonation wave propagating inside the detonation tube and given in Table 2, the cell sizes are on the order of 1-4 mm for the H_2-N_2O mixtures [40,41] and 1.5-2 mm for H_2-O_2-Ar mixtures [42,43]. The smallest characteristic dimension of spatial features on the OH fronts depends on the extent of instability. For highly unstable fronts, the distribution of scales has a fractal-like character [17,18,28,27], and the smallest scale can be as much as a factor of 50-100 times smaller than the largest scale.

One possible cause of the differences observed between Fig. 5 and 6 is the difference in mixture thermodynamic properties. The two cases have different propagation velocities, temperature, and species profiles within the reaction zones. As a consequence, the speed of propagation of signals within the reaction zone behind the leading shock front will differ for the two cases. This effect can be analyzed using an idealized model originally developed by Skews [44] for unreactive shock waves and applied to detonation waves by Gvozdeva [45] and Schultz [15]. The basis of this model is shown in Fig. 8 and uses geometric acoustics to track the wavefront of the disturbance created by the corner of the tube and exit plane. The disturbance speed v along the shock front can be computed by assuming that the signal from the corner is traveling radially into the shocked material at the local sound speed c while being convected downstream with the velocity u, the post-shock velocity in the lab

frame. From the geometry of Fig. 8, the angle α is determined by

$$\tan\alpha = \frac{v}{U_S} = \frac{\sqrt{c^2-(U_S-u)^2}}{U_S} = \frac{\sqrt{c^2-w^2}}{U_S}\,, \tag{1}$$

where w is the fluid velocity behind the shock in the shock-fixed frame, and U_S is the lead shock velocity. For diffraction from a round tube, a central disk-like portion (on the axis of symmetry) of the wavefront will remain undisturbed up to a distance x_c from the tube exit. At a distance x_c and time t_c, the corner signals generated along the circumference of the tube exit and traveling inward on the detonation front will meet. The distance x_c and time t_c at which the disturbance signal reaches the tube axis are

$$x_c = \frac{D}{2\tan\alpha}, \qquad t_c = \frac{D}{2\tan\alpha\, U_S}. \tag{2}$$

Evidence of the finite propagation speed of the corner disturbance into the reaction zone can be observed in the schlieren images, Fig. 5 and 6. In the case of a diffracting detonation [15] the disturbance propagation angle α is a strong function of position within the reaction zone and usually attains a maximum value some distance behind the front, Fig. 9. The maximum in α gives a lower bound for t_c and x_c, the time and distance at which the acoustic disturbance signal reaches the tube axis. Observations by Schultz [15] show that for irregular mixtures that are sufficiently subcritical, the boundary between the planar central region and the curved portion of the wavefront does indeed appear to move inward with a propagation speed consistent with the von Neumann state.

For the H_2-O_2-Ar, mixtures, the distance x_c is 40 mm throughout the induction zone. For the H_2-N_2O mixtures, the distance is 46 to 53 mm depending on the choice of α. The propagation of the corner signal and the location of the points x_c are shown graphically for both mixtures in Fig. 10a and b. Clearly the influence of thermodynamic properties cannot explain the persistence of the coupling between the reaction front and leading shock for the case of H_2-O_2-Ar since the distance x_c is smaller than in the case of H_2-N_2O. Another way of visualizing the difference in the failure process is in the normalized wavefront plot shown in Fig. 10c and d. In these plots, the location of the shock front is normalized by the location at the wall so that the shape will be hemispherical if the propagation speed is independent of location along the front. The H_2-N_2O case is clearly more quickly approaching a hemispherical shape than the H_2-O_2-Ar case. This is due to the more rapid decoupling of the reaction zone from the shock in the H_2-N_2O case which results in the cessation of conversion of chemical to thermal energy. The rapid cessation of chemical reaction during the diffraction process means that the expansion waves behind

the curved shock front will dominate the shock evolution (see the discussion in Arienti and Shepherd [23]) and cause the front to form a hemispherical shape.

4.2 Critical Regime - subcritical outcome.

To reach the critical regime, the amount of argon dilution is decreased or the initial pressure increased compared to the mixtures in the sub-critical regime. The differences between mixtures are most strikingly observed on images in the critical regime, contrast Fig. 11a-d and 11e-h. The experimental setup and acquisition of these images is identical to Fig. 7. Comparing these with Fig. 7, we see that for the H_2-N_2O mixture there is hardly any difference between the sub-critical regime and critical regime with sub-critical outcome. In case of detonation failure, the reaction front is coupled to the lead shock front in the critical regime at maximum about 45 mm from the tube exit plane, only slightly longer than the 40 mm observed in the sub-critical regime. On the multiple-exposure chemiluminescence images for H_2-N_2O, Fig. 11e, the cone-like boundary of the high-intensity region in the critical case is similar to the sub-critical case.

By contrast, the reaction front for the H_2-O_2-Ar mixture remains coupled to a portion of the shock front near the tube axis for much larger distance from the diffraction plane, as shown in Fig. 11c. Moving the ICCD camera field of view even further downstream, we find that the coupling persists over a portion of the wavefront up to 86 mm, as shown in Fig. 12c. On the enlargement shown in Fig. 13, we have labeled the important features and the portion of the reaction zone that remains coupled to the shock front can be clearly seen. On the multiple-exposure chemiluminescence images for H_2-O_2-Ar, Fig. 11a, the boundary of the high-intensity region in the critical case extends much further from the diffraction plane that in the sub-critical case, Fig. 7a.

4.3 Critical regime, supercritical outcome

These are all cases within the critical regime that result in a detonation eventually forming during the diffraction process. All of these events are characterized by decoupling of the shock and reaction front away from the tube axis followed by a re-initiation event, Fig. 14. The term re-initiation may be misleading since failure does not occur over the entire detonation front. In the present context, re-initiation means that a localized explosion occurs that results in the re-coupling of shock and reaction front that ultimately spreads over the entire front. Prior to the localized explosion event, the shocked but unburned reactants are located in a region best described as a thick spherical shell, which has been visualized using stereoscopic imaging [46]. The inner radius corresponds

to the distance from the tube exit plane center to the OH front, and the outer radius corresponds to the distance to the lead shock front. In a re-initiation event, a detonation advances transversely through the shocked reactants in the azimuthal and polar direction and completes the reaction in the shell-like region.

On schlieren images, the transverse detonation resulting from a re-initiation event is best visualized if located on the very top or bottom, since the three-dimensional masking effect is smallest there. A set of images showing several such re-initiation events is given in Fig. 15, the image acquisition is identical to that described for Figs. 7 and 11. At least two re-ignition events are observed to occur simultaneously in the chemiluminescence image of Fig. 15a. These are indicated by the set of concentric arcs of high luminosity originating in the shocked region off-axis where the initial decoupling takes place. The re-initiation events result in shock "bubbles" seen in the corresponding portions of the schlieren image shown in Fig 15b. An enlarged overlay is shown in Fig 15d, this was created from the PLIF image Fig 15e and the cropped schlieren image of Fig 15c. No PLIF luminosity can be observed from the OH regions associate with the re-initiation because the excitation light sheet does extend into these regions. An extended region of coupling between the shock and reaction zone is visible near the tube axis in Fig. 15d.

For a large number of experiments, the transverse detonation starts close to the edge of the coupled region at the leading reaction front and propagates "backward", i.e., toward the wall. These re-initiation events are remarkably similar in appearance to those computed by Arienti and Shepherd (see Fig. 15 and 16 of [23]), who found that for a sufficiently high activation energy, re-initiation took place off-axis through a detonation wave propagating into shocked but un-reacted gas and moving transversely to the leading shock front and moving from the head of the diffracted wave toward the wall. The re-initiation waves observed in [23] originated from a fold or kink in the shock front that developed due to a local maximum in pressure created by the interaction of expansion waves with the leading shock front.

For some experiments, the re-initiation event takes place further off the tube axis. In this case, the transverse detonation propagates through the decoupled region toward the leading front, which is clearly coupled as observed on the schlieren-PLIF overlay images (Fig 15). The re-ignition events observed for the H_2-N_2O mixtures are similar to the ones for the Ar-diluted mixtures. Note that the transverse detonation is not always successful and in rare occasions is observed to fail, a fact also seen for cylindrically expanding detonations [4]. In such a case, re-coupling of the detonation is achieved by further transverse detonations which are initiated from multiple simultaneous re-ignition events.

4.4 Axial velocity decay

In order to quantify the differences in the decoupling processes of the two mixture types, multiple exposure images were analyzed to determine the velocity profile of the reaction front near the centerline. A 20-pixel-wide (about 5 mm) horizontal stripe, centered on the tube axis, was extracted from each chemiluminescence image. The pixel counts on the stripe were then averaged in the direction perpendicular to the tube axis in order to obtain a smooth, one-dimensional intensity profile. The position of the maximum gradient in intensity was taken to be the location of the chemiluminescence front. The velocity is computed from the displacement of the front on sequential images divided by the time between the images. The uncertainty in location for the front of $\pm$ one pixel implies an uncertainty of $\pm$75 m/s in velocity for the smallest time increment of 6 μs [47].

Immediately after the detonation wave exits the tube, the velocity of the central portion of the detonation front is within 5% of the CJ velocity since the corner disturbance signal from the abrupt area change has not reached the tube axis. For detonation velocities close to the CJ velocity, the reaction front is sufficiently close to the leading shock front that within the resolution and alignment of the imaging system, they appear to coincide. The velocity of the chemiluminescence front derived from multiple exposure images, Fig 16, was within 5% of the calculated CJ velocity up to distances x_{TEP} <30 mm from the tube exit plane in all experiments conducted.

For the sub-critical cases of the H_2-O_2-Ar dilution series, the axial velocity is greater than 0.9 U_{CJ} and is fairly constant for $x < 44$ mm. The axial velocity is greater than 80% of U_{CJ} for $x \leq 64$ mm. In the last 20 mm of propagation, the velocity suddenly decreases to 0.5–0.6 U_{CJ}. For the sub-critical cases of the Htw-N_2O series there is a slow decay in the axial reaction front velocity up to a distance of 34 mm for which the minimum velocity measured was 0.94 U_{CJ}. After that distance, a drastic fall-off in velocity is observed. Within 17 mm, the reaction front slows down to 0.25–0.55 U_{CJ}.

For the super-critical cases of the Ar series, the velocity is larger than 0.9 U_{CJ} up to x_{TEP} =52 mm . For larger distances, velocities of 0.7–1 U_{CJ} are measured. The velocity data obtained at large distances from the tube end plate are not all close to the CJ value since the re-initiation event may have happened off axis or the last exposure took place before the re-ignition event. For the super-critical cases of the N_2O series, the velocity profiles for $x_{TEP} < 32$ mm are essentially unaltered from the sub-critical cases. The two data points appearing for $U/U_{CJ}< 0.7$ were identified as cases where the re-initiation has taken place off the tube axis. In these events, velocity increases and was measured to be as high as 1.05 U_{CJ} at $x_{TEP} = 70$ mm.

We propose that the difference in behavior between the H_2-O_2-Ar (Fig 16a) and H_2-N_2O (Fig 16c) subcritical cases can be primarily explained by considering the interaction of the reaction zone and the expansion wave generated by the diffraction process [16,23]. As the expansion waves from the corner reach the centerline and the lead shock begins to decay, the reaction zone starts to recede from the shock front. This can be seen most clearly in the time-distance diagrams of Fig. 17 which were obtained by analyzing the simultaneous imaging of the shock and reaction zone. The near coincidence of shock and reaction front location close to the exit plane indicate coupling between shock and reaction front location until a distance of $x_{TEP} \approx 60$ mm for the Ar-diluted mixture and $x_{TEP} \approx 40$ mm in the case of the H_2-N_2O mixture. The recession of the reaction front from the shock can be explained by considering [16,23] the effect of slight unsteadiness on the reaction. Small decreases in shock velocity have a large effect for high activation energy mixtures and as shown in computations [16,23] can lead to extinction of the reaction process. This in turn results in rapid shock decay since the chemical energy ceases to be converted into the thermal energy that is sustaining the shock motion in the detonation process. The consequence is the same in both mixtures but occurs much closer to the exit plane in the H_2-N_2O mixture than for the H_2-O_2-Ar mixture. This is consistent with the critical decay rate model and the difference in critical decay times (computed as described in Section 3 and given in Table 2) for the two mixtures.

5 Conclusions

The differences in the detonation diffraction processes in highly argon diluted H_2-O_2 mixtures with regular structure and highly irregular H_2-N_2O mixtures were documented qualitatively in and close to the critical regime. The mixtures studied have normalized effective activation energies at CJ conditions of $\theta = 4.5$ and 9.4 respectively, and represent examples of mixtures with regular and highly irregular instability structures. This classification is consistent with the stability parameter χ [21] defined as the ratio of induction length Δ_i to energy pulse length Δ_e. For the H_2-O_2-Ar and H_2-N_2Omixtures χ was calculated to be 9.3 and 36 respectively. Depending on the diffraction regime, different modes have been identified and quantified for each mixture type. The differences were most striking in the sub-critical and especially in the critical regime, for cases in which the detonation wave fails. For the first time, the reaction front has been directly visualized for a diffracting detonation using PLIF of the OH radical, clearly showing the details of the reaction front.

For the low-activation-energy mixture and sub-critical outcome, the reaction front velocity on the center line decays significantly slower than in the high-activation-energy case. In some sub-critical cases, the reaction front remained

attached to the lead shock up to 2.3 tube diameters d from the tube end plate (Fig. 12c and 13). The reaction front velocity on the center line was above 0.8 U_{CJ} up to approximately 1.5d from the tube exit. For the H_2-N_2O mixture, the reaction front velocity decreased to approximately 0.6 U_{CJ} after a distance of 1.1 d. The reaction front decoupled fairly rapidly over the entire shock surface for the H_2-N_2O mixtures, leading shortly after the tube exit to a self-similar shape of the hemispherical shock. The rapid decay of the reaction front velocity can be attributed to the higher activation energy of the H_2-N_2O mixture, as compared to the Ar-diluted case small changes in lead shock strength lead to large changes in the induction time.

The disturbance signal originating from the sudden expansion at the tube exit was analyzed using a simplified geometric acoustics model. The analysis revealed that the distinctive diffraction behavior cannot be attributed to differences in thermodynamic properties between both mixture types. Instead, we propose that these differences are associated with the substantially larger effective activation energy for the H_2-N_2O case as compared to the H_2-O_2-Ar mixture. This proposal is consistent with the critical decay rate model of Eckett et al. [16] and the analysis of detonation diffraction by Arienti and Shepherd [23]. Arienti and Shepherd's computations did not include transverse waves in the initial detonation but found behavior very analogous to the present experimental results. This suggests that the interaction of the corner expansion waves with the reaction zone and the effect of unsteadiness on the reaction process is as important or more so than the interaction of transverse waves.

Acknowledgments

This work was supported by the US DOE, NNSA through the Caltech ASC Alliance Program, Center for Simulation of Dynamic Response of Materials under U. S. Department of Energy contract W-7405-ENG-48 and also the Office of Naval Research Grants Pulse Detonation Engines: Initiation, Propagation and Performance and Multidisciplinary Study of Pulse Detonation Engines. We thank Princeton Instruments for the loan of the ICCD camera used to take the multiple exposure chemiluminescence images.

References

[1] A. N. Dremin, V. S. Trofimov, *Proc. Combust. Inst.* 10 (1965) 839–843.

[2] Y. B. Zeldovich, S. M. Kogarko, N. N. Simonov, *Sov. Phys. Tech. Phys.* 1 (8) (1956) 1689–1713.

[3] V. V. Mitrofanov, R. I. Soloukhin, *Soviet Physics-Doklady* 9(12) (1965) 1055–1058.

[4] D. H. Edwards, G. O. Thomas, M. A. Nettleton, *J. Fluid Mech.* 95 (1979) 79–96.

[5] H. Matsui, J. H. S. Lee, *Proc. Combust. Inst.* 17 (1979) 1269–1280.

[6] J. H. S. Lee, *Ann. Rev. Fluid Mech.* 16 (1984) 311–336.

[7] J. H. S. Lee, *The Detonation Phenomenon*, Cambridge University Press, 2008.

[8] R. Knystautas, J. H. S. Lee, C. M. Guirao, *Combust. Flame* 48 (1) (1982) 63–83.

[9] C. K. Westbrook, P. A. Urtiew, *Proc. Combust. Inst.* 19 (1982) 615–623.

[10] I. O. Moen, A. Sulmistras, G. O. Thomas, D. Bjerketvedt, P. A. Thibault, *Prog. Astronaut. Aeronaut.* 106 (1986) 220–243.

[11] J. E. Shepherd, I. O. Moen, S. B. Murray, P. A. Thibault, *Proc. Combust. Inst.* 21 (1986) 1649–1658.

[12] D. Desbordes, *Prog. Astronaut. Aeronaut.* 114 (1988) 170–185.

[13] D. Desbordes, *Prog. Astronaut. Aeronaut.* 153 (1995) 347–359.

[14] J. S. Lee, in: J. Bowen (Ed.), Dynamics of Exothermicity, Gordon and Breach, Amsterdam, Netherlands, 1996, pp. 321–336.

[15] E. Schultz, *Detonation Diffraction Through an Abrupt Area Expansion*, Ph.D. thesis, California Institute of Technology (2000).

[16] C. A. Eckett, J. J. Quirk, J. E. Shepherd, *J. Fluid Mech.* 421 (2000) 147–183.

[17] F. Pintgen, J. M. Austin, J. E. Shepherd, in: G. Roy, S. Frolov, R. Santoro, S. Tsyganov (Eds.), Confined Detonations and Pulse Detonation Engines, Torus Press, Moscow, 2003, pp. 105–116.

[18] F. Pintgen, J. E. Shepherd, in: G. D. Roy, S. M. Frolov, J. E. Shepherd (Eds.), Application of Detonation to Propulsion, Torus Press, Moscow, 2004, pp. 105–116, iSBN 5-94588-025-6.

[19] R. A. Strehlow, *Combust. Flame* 12 (1968) 81–101.

[20] V. Y. Ul'yanitskii, *Combustion, Explosion and Shock Waves* 17 (2) (1981) 227–232.

[21] H. D. Ng, M. I. Radulescu, A. J. Higgins, N. Nikiforakis, J. H. S. Lee, *Combust. Theor. Model.* 9 (3) (2005) 385–401.

[22] Z. Liang, S. Browne, R. Deiterding, J. E. Shepherd, *Proc. Combust. Inst.* 31 (2007) 2445–2453.

[23] M. Arienti, J. E. Shepherd, *J. Fluid Mech.* 529 (2005) 117 – 146.

[24] E. G. Pantow, M. Fischer, T. Kratzel, *Shock Waves* 6 (1996) 119–129.

[25] D. A. Jones, G. Kemister, E. S. Oran, M. Sichel, *Shock Waves* 6 (1996) 119–129.

[26] D. H. Edwards, G. Hooper, G. O. Thomas, *Journal of Physics D: Applied Physics* 14 (1981) 833–840.

[27] J. M. Austin, F. Pintgen, J. E. Shepherd, *Proc. Combust. Inst.* 30 (2005) 2735–2742.

[28] F. Pintgen, *Detonation Diffraction in Mixtures with Various Degrees of Regularity*, Ph.D. thesis, California Institute of Technology (December 2004).

[29] F. Pintgen, *Laser-Optical Visualization of Detonation Structures*, Diplomarbeit, Lehrstuhl für Thermodynamik: Technische Universität München / Graduate Aeronautical Laboratories: California Institute of Technology, Munich, Germany (December 2000).

[30] F. Pintgen, C. A. Eckett, J. M. Austin, J. E. Shepherd, *Combust. Flame* 133 (3) (2003) 211–229.

[31] M. J. Kaneshige, *Gaseous detonation initiation and stabilization by hypervelocity projectiles*, Ph.D. thesis, California Institute of Technology, Pasadena, California (January 1999).

[32] R. Akbar, *Mach Reflection of Gaseous Detonations*, Ph.D. thesis, Rensselaer Polytechnic Institute, Troy, NY (August 1997).

[33] R. A. Strehlow, *Astronautica Acta* 15 (1970) 345–357.

[34] J. Libouton, A. Jacques, P. V. Tiggelen, *Actes du Colloque International Berthelot-Vieille-Mallard-Le Chatelier* 2 (1981) 437–442, Bordeaux.

[35] J. E. Shepherd, *Prog. Astronaut. Aeronaut.* 106 (1986) 263–293.

[36] U. Maas, J. Warnatz, *Combust. and Flame* 74 (1988) 53.

[37] M. Mueller, R. Yetter, F. Dryer, *Int. J. Chem. Kinetics* 32 (6) (2000) 317–339.

[38] M. Short, *J. Fluid Mech.* 430 (2001) 381–400.

[39] M. Short, G. J. Sharpe, *Combust. Theor. Model.* 7 (2) (2003) 401–416.

[40] R. Akbar, M. Kaneshige, E. Schultz, J. E. Shepherd, *Detonations in H_2–N_2O–CH_4–NH_3–O_2–N_2 Mixtures*, Tech. Rep. FM97-3, Graduate Aeronautical Laboratories at California Institute of Technology (1997).

[41] U. Pfahl, E. Schultz, J. E. Shepherd, *Detonation Cell Width Measurements for H_2-N_2O-O_2-CH_4-NH_3 Mixtures*, Tech. Rep. FM98-5, GALCIT (April 1998).

[42] R. A. Strehlow, R. Liangminas, R. H. Watson, J. R. Eyman, *Proc. Combust. Inst.* 11 (1967) 683–692.

[43] J. M. Austin, *The Role of Instability in Gaseous Detonation*, Ph.D. thesis, California Institute of Technology, Pasadena, California (June 2003).

[44] B. Skews, *J. Fluid Mech.* 29 (1967) 297–304.

[45] T. V. Bazhenova, L. G. Gvozdeva, Y. S. Lobastov, I. M. Naboko, R. G. Nemkov, O. A. Predvoditeleva, *Shock waves in real gases*, Tech. Rep. TT-F-58, NASA Technical Translation (1969).

[46] F. Pintgen, J. E. Shepherd, *J. Flow Visualization and Imaging Processing* 14 (2007) 121–142.

[47] F. Pintgen, *Detonation diffraction in mixtures with various degrees of instability*, Ph.D. thesis, California Institute of Technology, Pasadena, California (Dec 2004).

	mixture	P_0 (kPa)	β	Δ_i (mm)	θ	number of shots
Ar dilution series	$2H_2+O_2+\beta Ar$	100	3–8.6	0.57–0.113	4.8–5	77
Ar pressure series	$2H_2+O_2+3Ar$	45–100	-	0.48–0.114	4.7–5	19
N_2O series	H_2+N_2O	40–80	-	0.95–0.178	9.4–9.6	71

Table 1
Summary of parameters and test conditions.

composition	P_0	β	λ	D/Δ	D/λ	Δ_i/Δ_e	$t_{d,c}$
	(kPA)		(mm)				(μs)
$2H_2+1O_2+\beta$ Ar	100	5.8–6.4	1.5–2	556–516	19-25	1.9	0.81
H_2+N_2O	42–48	-	1–4	226–250	10–38	3.8	2.5

Table 2
Critical regime parameters.

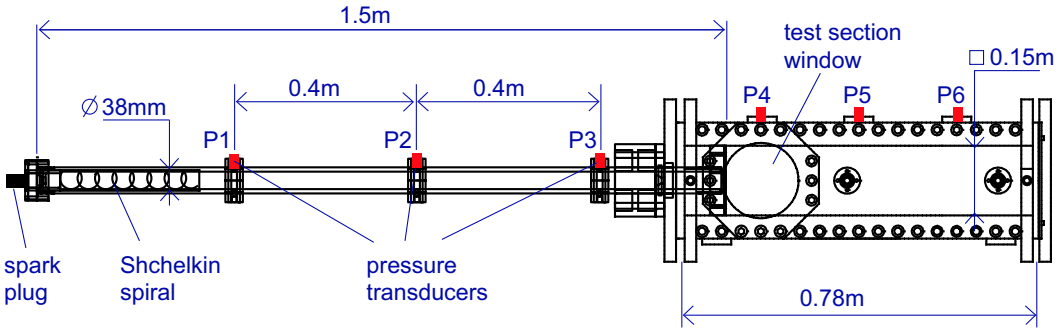

Fig. 1. Schematic of detonation diffraction tube [15].

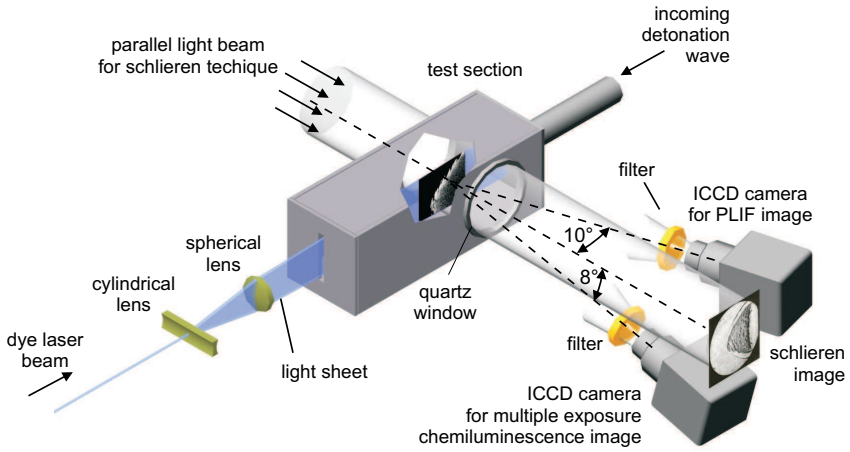

Fig. 2. Schematic of setup used for obtaining simultaneous PLIF, schlieren and chemiluminescence images.

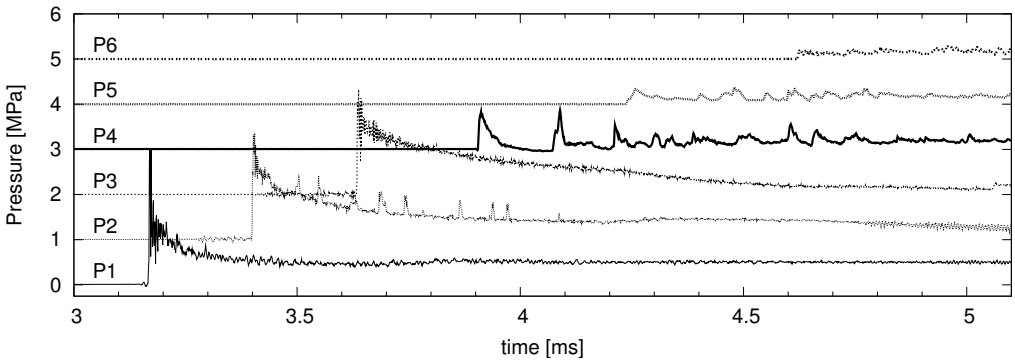

a)

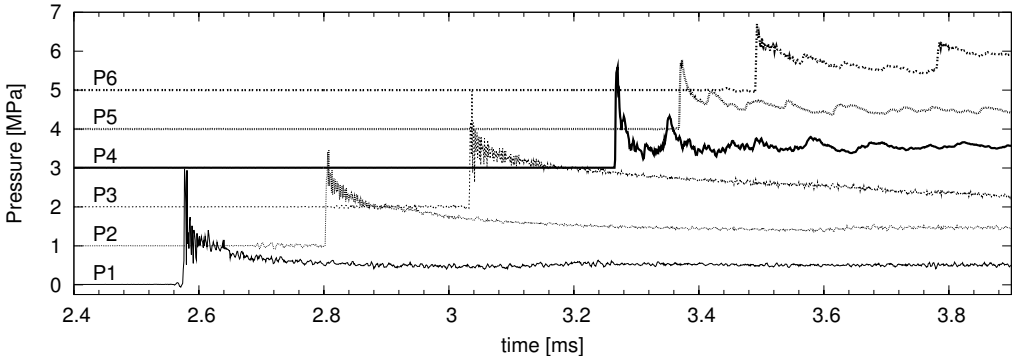

b)

Fig. 3. Pressure traces. a) Sub-critical. 0.213 H_2 + 0.107 O_2 + 0.68 Ar, $P_0 = 100$ kPa. b) Super-critical. 0.233 H_2 + 0.117 O_2 + 0.65 Ar, $P_0 = 100$ kPa.

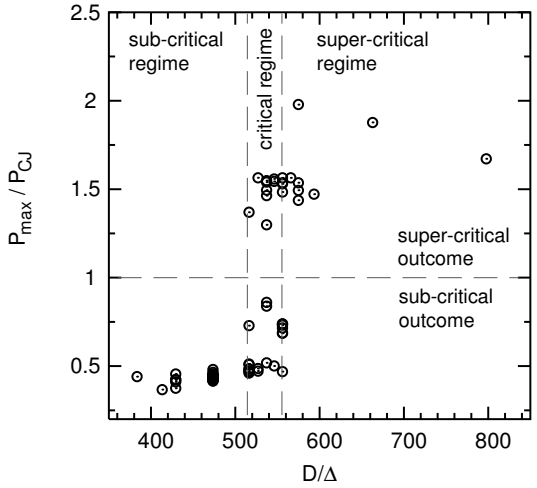

Fig. 4. Identification of critical regime for Ar-diluted H_2-O_2 mixtures. Summary of all tests in the dilution series plotted in terms of normalized coordinates $P_{4,max}/P_{CJ}$ and D/Δ_i. The maximum pressure at P_4 is measured within 100 μs of the initial rise.

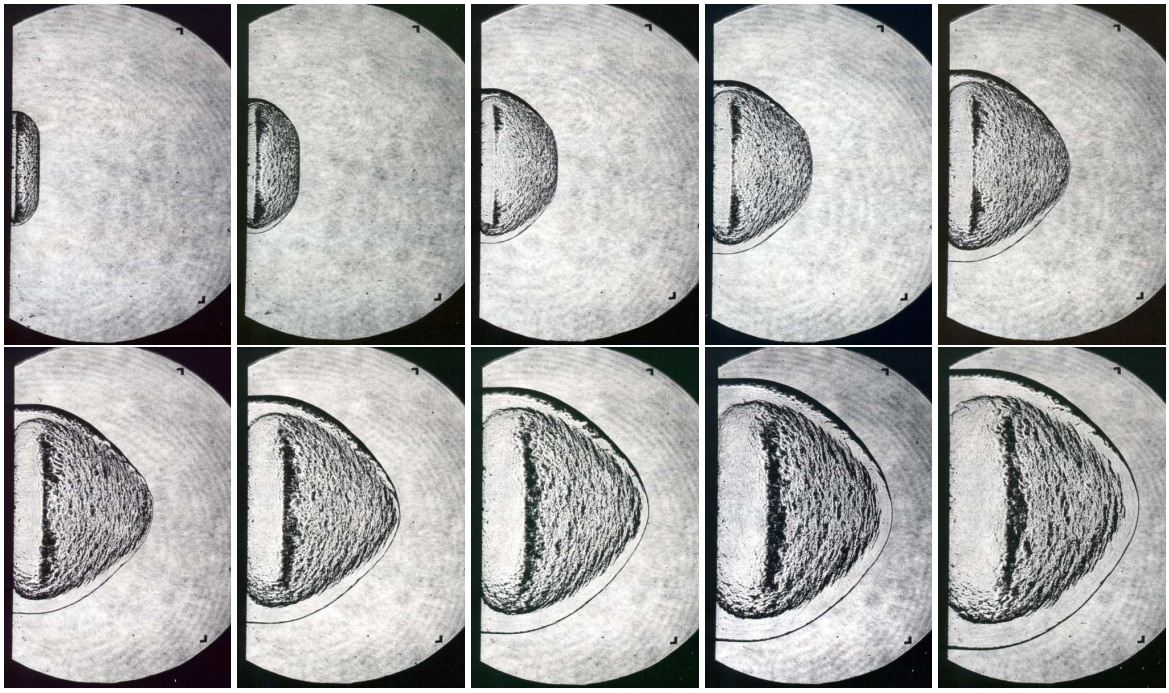

Fig. 5. Schlieren images obtained from 10 separate experiments in the subcritical regime using the same $0.2H_2+0.1O_2+0.7Ar$ mixture and initial conditions of $P_0 =$ 100 kPa.

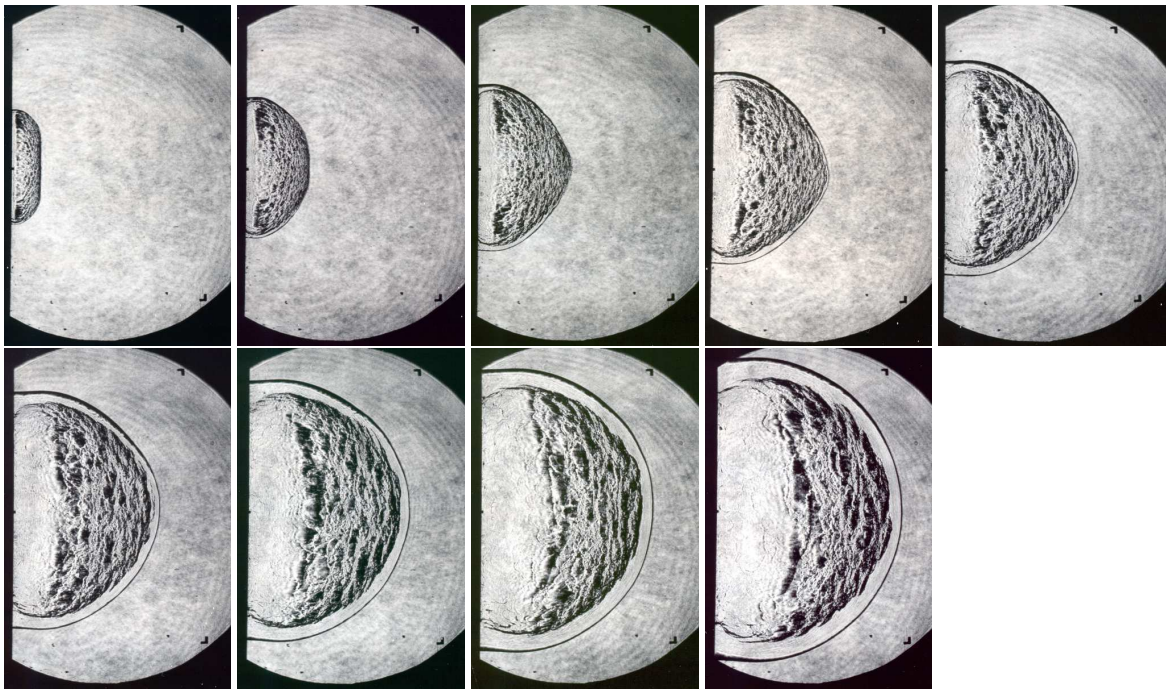

Fig. 6. Schlieren images obtained from nine separate experiments in the subcritical regime using the same $0.5H_2{+}0.5N_2O$ mixture and initial conditions of $P_0 = 40$ kPa.

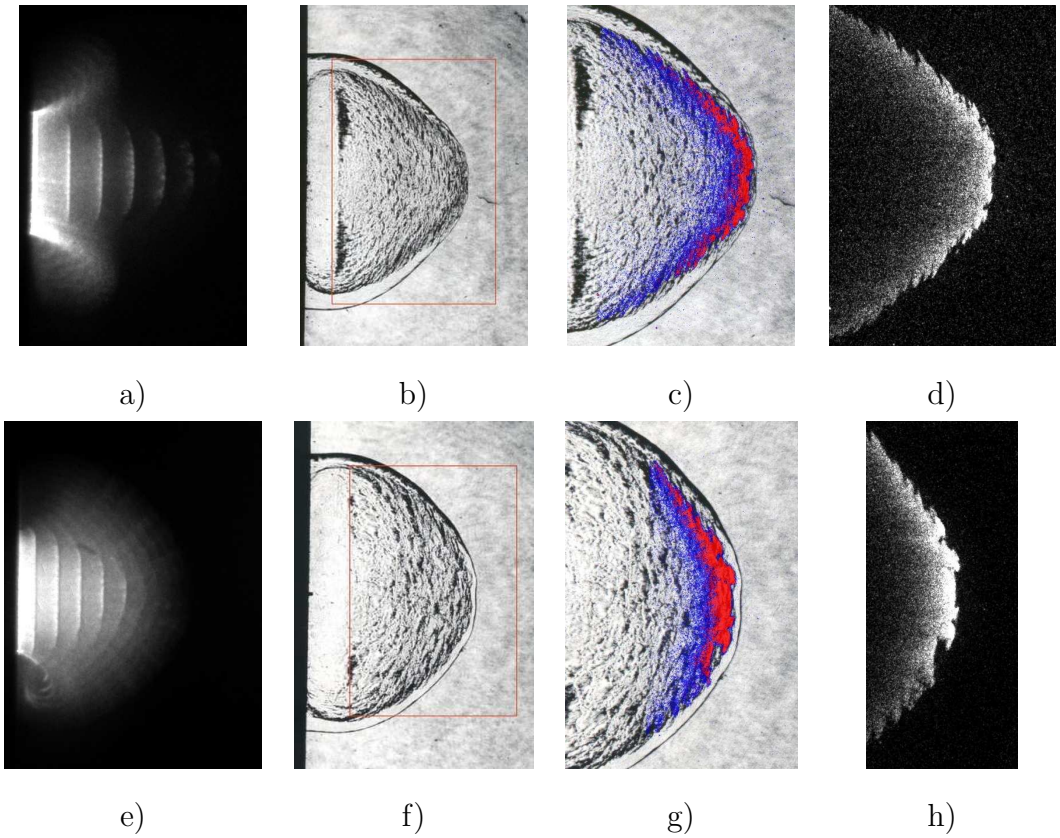

Fig. 7. Observations in the sub-critical regime: a)-d) Ar-diluted mixture. e)-h) H_2-N_2O mixture.

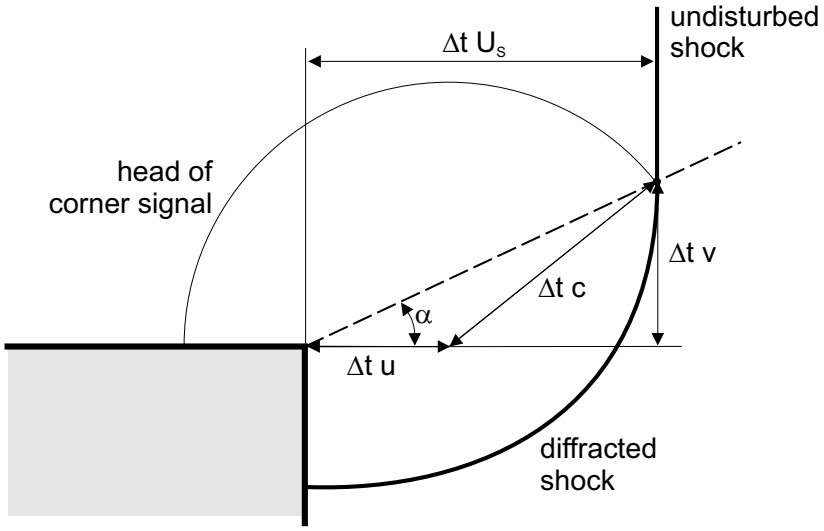

Fig. 8. Skews' construction of disturbance propagation from corner along the shock front.

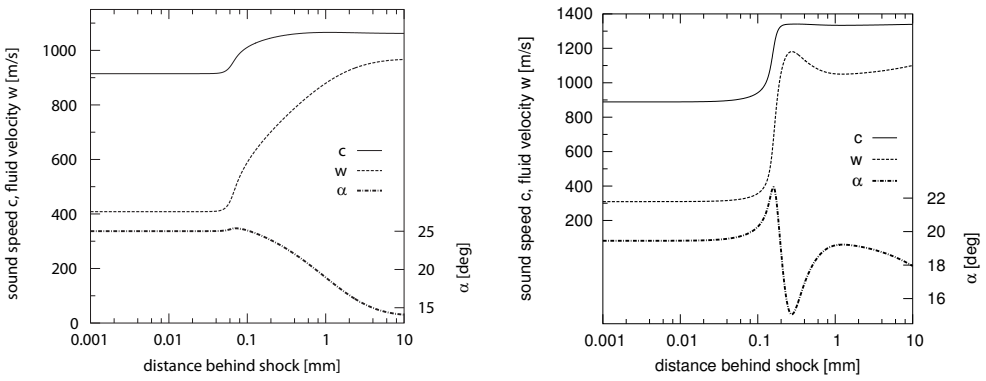

Fig. 9. Local sound speed, fluid velocity, and disturbance propagation angle α calculated with the ZND-CJ model. a) $0.233H_2$+$0.117O_2$+0.65Ar, P_0 = 100 kPa, Maas-Warnatz [36] mechanism. b) $0.5H_2$+$0.5N_2O$, P_0 = 45 kPa, Mueller [37] mechanism.

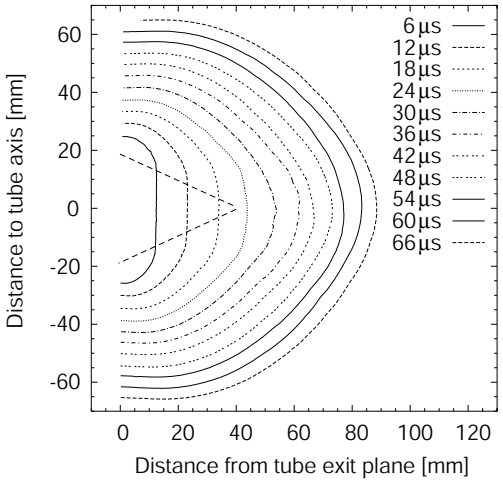

a) $2H_2$+O_2+7Ar, $P_0 = 1$ bar

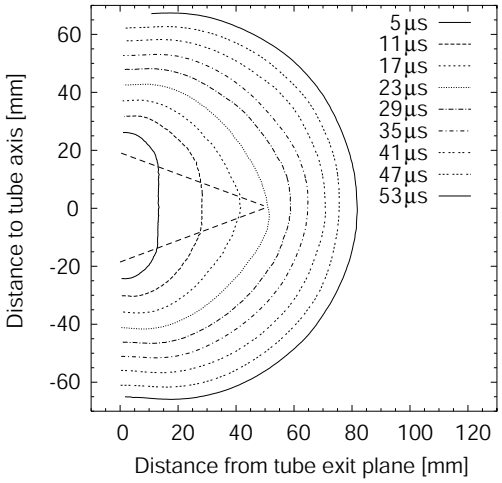

b) H_2+N_2O, $P_0 = 0.4$ bar.

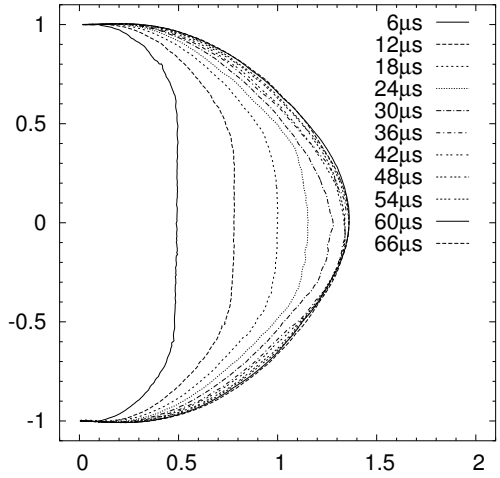

c) $2H_2$+O_2+7Ar, $P_0 = 1$ bar

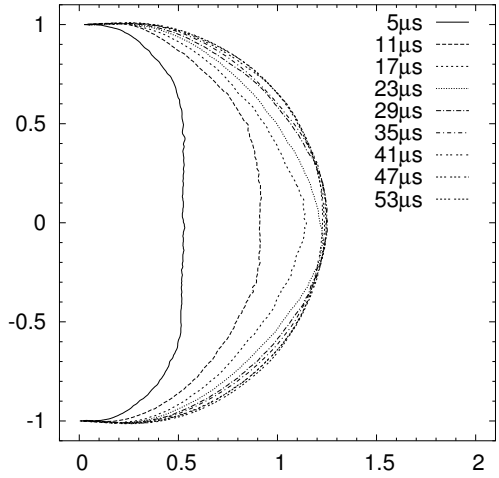

d) H_2+N_2O, $P_0 = 0.4$ bar.

Fig. 10. a) and b) Edge-detected leading shock front from multiple schlieren images in lab coordinates and c) and d) normalized to the shock location at the wall. The locus of corner disturbance signals based on Skews' construction are shown in a) and b).

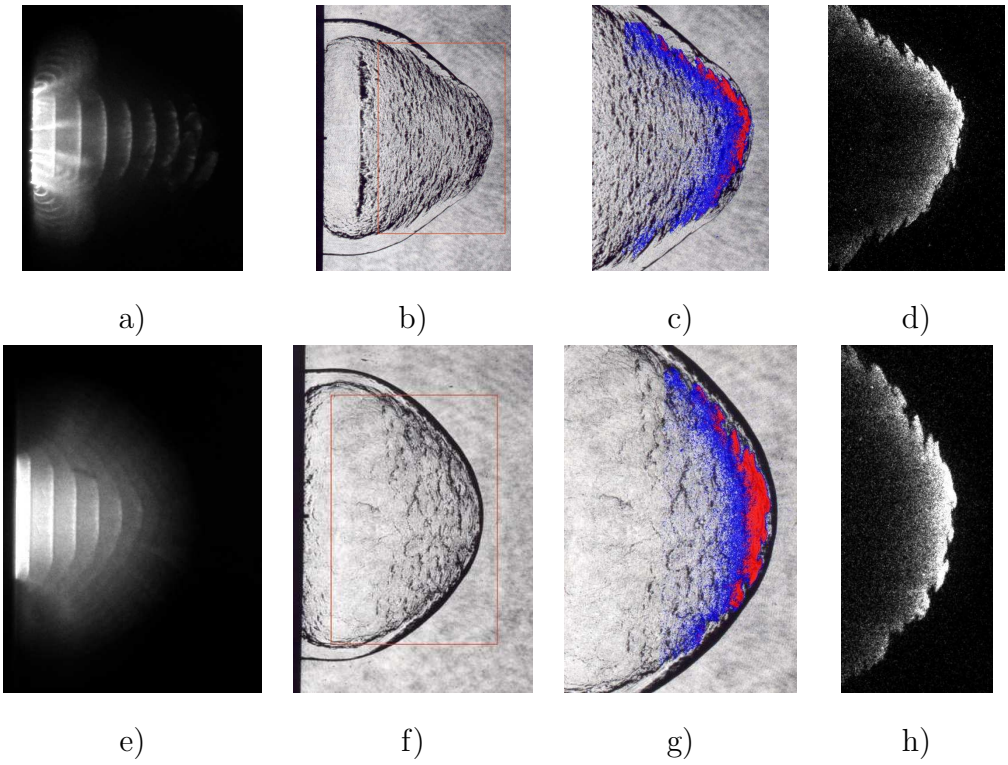

Fig. 11. Observations in the critical regime: a)-d) Ar-diluted mixture. e)-h) H_2-N_2O mixture.

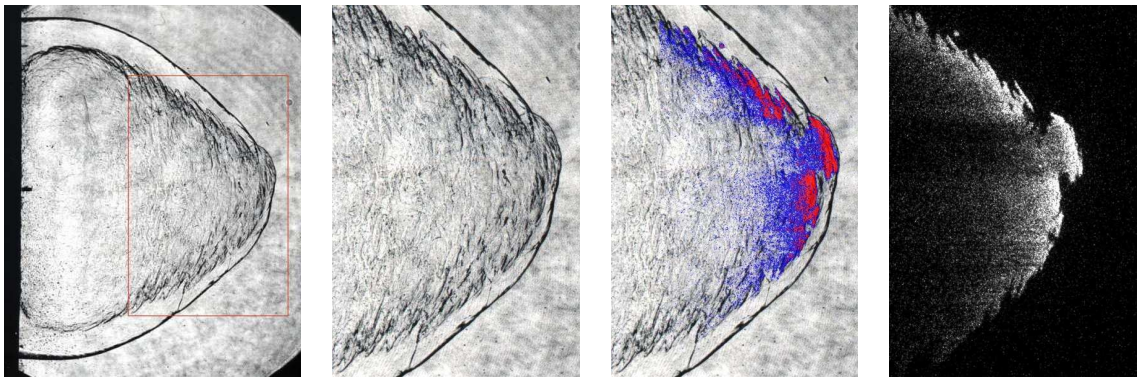

a) b) c) d)

Fig. 12. Keystones of higher fluorescence coupled to shock front observed far from tube exit. 0.22 H_2 + 0.11 O_2 + 0.67 Ar, P_0 = 100 kPa. Schlieren image (a) height: 125 mm.

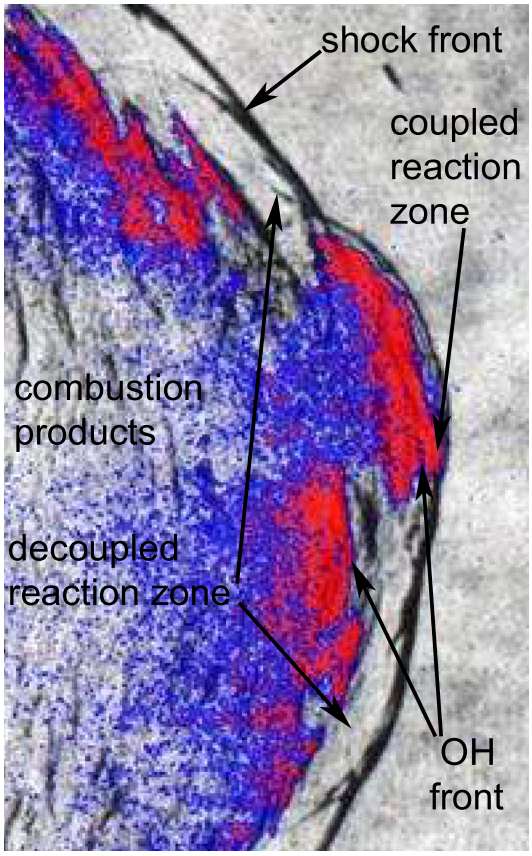

Fig. 13. Enlarged portion of Fig. 12c showing the coupled portion of the reaction zone surrounded by decoupled regions.

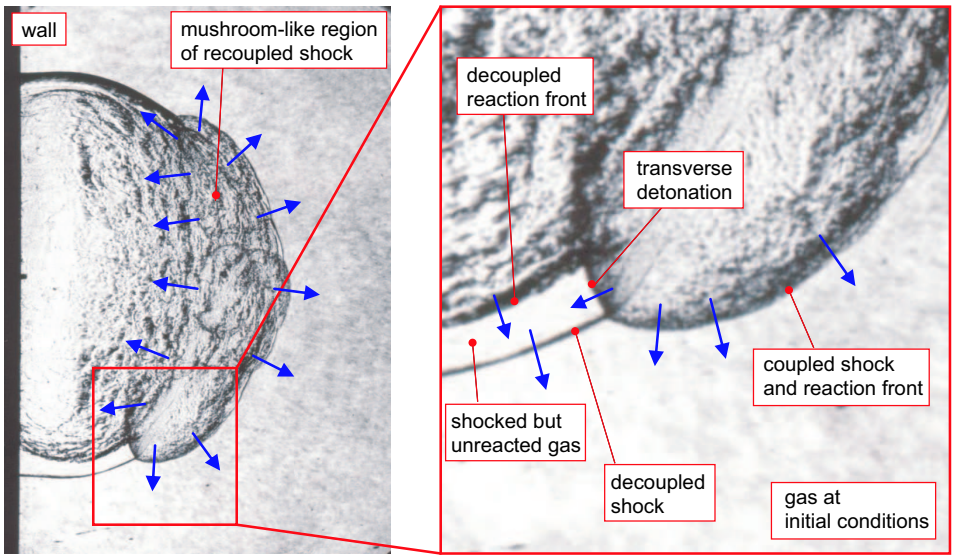

Fig. 14. Re-initiation event and detailed view of transverse detonation, 0.5 H_2 + 0.5 N_2O, $P_0 = 45$ kPa. Blue arrows indicate the propagation direction of the detonation fronts.

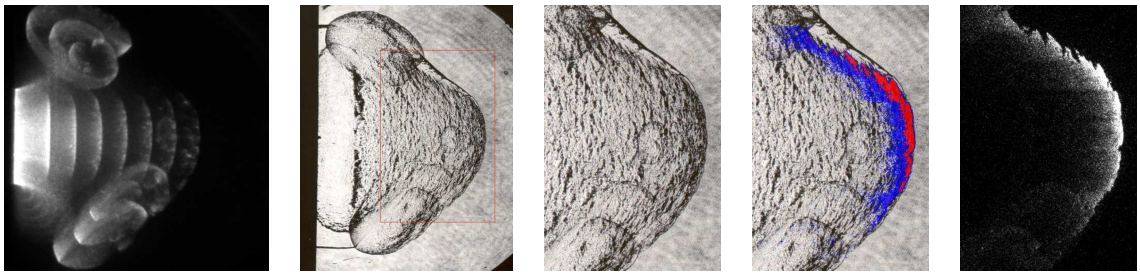

a) b) c) d) e)

Fig. 15. Reinitiation event for 0.24 H_2 + 0.12 O_2 + 0.64 Ar, $P_0 = 100$ kPa. Chemiluminescence image height: 109 mm, multiple gates delay: 7×6 μs. PLIF image height 70 mm.

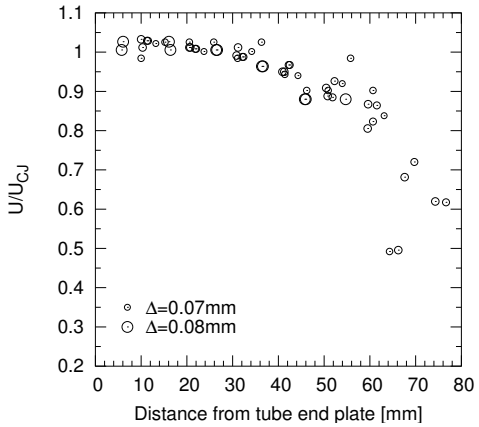

a) H_2-O_2-Ar, sub-critical outcome.

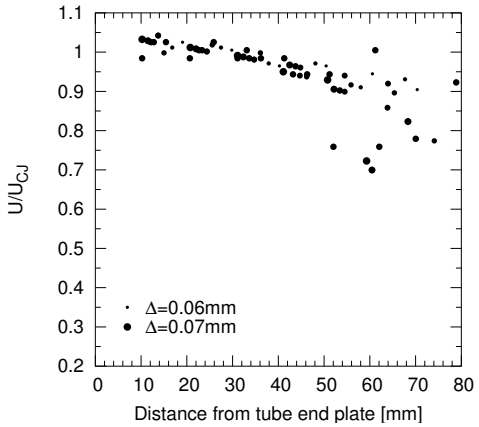

b) H_2-O_2-Ar, super-critical outcome.

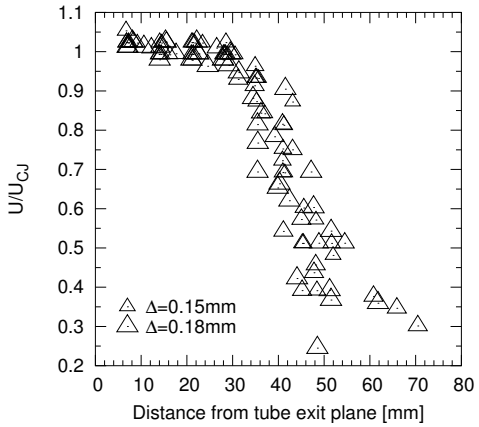

c) H_2-N_2O, sub-critical outcome.

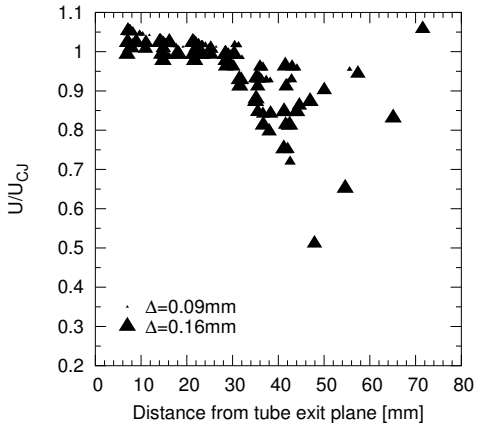

d) H_2-N_2O, super-critical outcome.

Fig. 16. Reaction front velocities from multiple exposure images versus distance from tube exit. Size of symbols is proportional to induction zone length at CJ conditions.

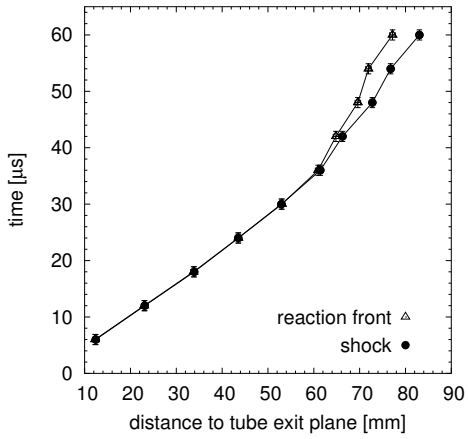

a)

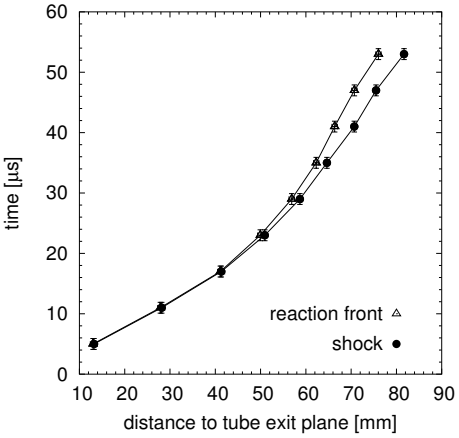

b

Fig. 17. Location of the shock and reaction front on tube centerline. a) $2H_2+O_2+7Ar$, $P_0 = 1$ bar and b) H_2+N_2O, $P_0 = 0.4$ bar.